Published in Journal of Neuroscience 2005, 25(1): 96-107

DEVELOPMENTAL CHANGES IN PARVALBUMIN REGULATE PRESYNAPTIC Ca^{2+} SIGNALING

T. Collin, M. Chat, M.G. Lucas, H. Moreno[1], P. Racay[2,3], B. Schwaller[2], A. Marty and I. Llano

Laboratory of Cerebral Physiology, CNRS, University Paris 5, 45 rue des Saints Pères, 75006 Paris, France, [1]Gertrude H Sergievsky and Taub Center for Alzheimer Research, Columbia University, New York, USA, [2] Division of Histology , Department of Medicine, University of Fribourg, 14, chemin du Musée, Fribourg, Switzerland, [3] Comenius University, Jessenius Faculty of Medicine, Institute of Biochemistry, Mala Hora 4, SK-03601 Martin, Slovak Republik

Abbreviated Title: Parvalbumin shapes presynaptic Ca_i dynamics

Corresponding author: Isabel Llano

Laboratory of Cerebral Physiology, CNRS, University Paris 5

45 rue des Saints Pères, 75006 Paris, France

e-mail: isabel.llano@univ-paris5.fr

Number of figures: 6

Number of tables: 1

Number of pages: 39

keywords: calcium, synapses, cerebellum, patch-clamp, imaging, development

Acknowledgments: We thank Yusuf P. Tan for support on optical engineering and analysis software and David DiGregorio for comments on the manuscript. Supported by grants from the French ministry of Scientific Research (ACI "Biologie du Développement et Physiologie Intégrative"), the Région Ile de France (Sésame Programme), the Swiss

National Science Foundation grants 3100-063448.00/1 and 3100A0-100400/1 (to B. S.) and an HFSP short-term fellowship to H. Moreno.

Abstract

Certain interneurons contain large concentrations of specific Ca^{2+}-binding proteins (CBP) but consequences on presynaptic Ca^{2+} signaling are poorly understood. Here we show that expression of the slow CBP parvalbumin (PV) in cerebellar interneurons is cell-specific and developmentally regulated, leading to characteristic changes in presynaptic Ca^{2+} dynamics (Ca_i). Using whole-cell recording and fluorescence imaging, we studied action potential evoked Ca_i transients in axons of GABA-releasing interneurons from mouse cerebellum. At early developmental stages (PN10-12), decay kinetics were significantly faster for basket than for stellate cells, whereas at PN19-21 both interneurons displayed fast decay kinetics. Biochemical and immunocytochemical analysis showed parallel changes in the expression levels and cellular distribution of PV. By comparing wild-type and PV(-/-) mice, PV was shown to accelerate the initial decay of action potential-evoked Ca_i signals in single varicosities, and to introduce an additional slow phase which summates during bursts of action potentials. The fast initial Ca_i decay accounts for an earlier report that PV elimination favors synaptic facilitation. The slow decay component is responsible for a pronounced, PV-dependent, delayed transmitter release which we describe here at interneuron-interneuron synapses following presynaptic bursts of action potentials. Numerical simulations account for the effect of PV on Ca_i kinetics, allow estimates for the axonal PV concentration (150 μM) and predict the time course of volume-averaged Ca_i in the absence of exogenous buffer. Overall, PV arises as a major contributor to presynaptic Ca_i

signals and synaptic integration in the cerebellar cortex.

In small mammalian synaptic terminals, Ca^{2+} concentration gradients subside on a time scale of the order of 1 ms, after which the Ca^{2+} concentration may be considered homogeneous (review: Meinrenken et al., 2003), as predicted from early work on squid axon (Simon and Llinas, 1985; Llinas et al., 1992). Therefore, volume-averaged Ca^{2+} measurements on single terminals give valuable recordings of the Ca^{2+} concentration intervening $\geq$ 1 ms after action potential-induced Ca^{2+}entry. This signal is called "$[Ca^{2+}]_{volumeavg}$" by Meinrenken et al. (2003), and is designated as Ca_i hereafter for simplicity. It has attracted comparatively little attention, probably because it is not directly related to phasic neurotransmitter release. It carries however much physiological significance. The elevated Ca_i that follows one or several action potentials contributes to setting the duration of the after spike hyperpolarization and hence the maximum firing frequency of the presynaptic terminal (review: Rudy et al., 1999). It is responsible for delayed transmitter release and facilitation (Goda and Stevens, 1994; Atluri and Regehr, 1998; Felmy et al., 2003; reviews: Van der Kloot and Molgo, 1993; Zucker and Regehr, 2002), and it may influence the kinetics of vesicle recycling (e.g., Smith et al., 1998; Burrone et al., 2002).

Measurements of Ca_i are affected by the presence of the Ca^{2+} probe, which acts as a buffer, as well as by the concentration and binding properties of endogenous buffers (review: Neher, 1998). Certain neurons are known to possess large concentrations of specific Ca^{2+} binding proteins (CBPs) such as calbindin D-28k (CB), calretinin (CR) or parvalbumin (PV), but the consequences of having one rather than the other on

presynaptic Ca_i dynamics are unknown. Effects of CBPs on synaptic transmission are just starting to be considered (Edmonds et al., 2000; Blatow et al., 2003; reviewed by Schwaller et al., 2002).

PV is a particularly interesting case. Because the two EF-hand domains of PV have a high affinity for Mg^{2+}, it has a slow apparent binding rate with Ca^{2+} (Lee et al., 2000). Moreover, PV displays a rather slow dissociation rate with Ca^{2+}. It can be predicted that PV should not affect much the fast Ca^{2+} signal responsible for phasic neurotransmitter release, and that it may act specifically on the slower processes governed by Ca_i. It was shown that at basket cell-Purkinje cell synapses, which contain PV presynaptically (Celio, 1986; Meyer et al., 2002), elimination of PV converts a depressing synapse into a facilitating one and it was suggested that PV reduces paired pulse facilitation by altering presynaptic Ca_i kinetics (Caillard et al., 2000). We have tested this prediction in the present work by comparing the time course of action potential-evoked Ca_i transients in single basket and stellate cell terminals under different conditions. We found characteristic biphasic decay kinetics associated with the presence of this CBP, which explain not only the previously found effect of PV deletion on facilitation, but also a newly uncovered effect of PV elimination on delayed transmitter release.

Materials and Methods

Preparation and solutions

Sagittal cerebellar slices (180 μm thick) were prepared as previously described (Llano et al., 1991) following decapitation after cervical dislocation, from wild-type (C57 Black 6 strain; called hereon WT) and PV(-/-) mice, raised on the same C57 background.

Two different age groups were studied: PN10-12 : 10 to 12 days postnatal and PN19-21 : 19 to 21 days postnatal. Experiments were done at 20-23°C in interneurons of the cerebellar molecular layer (MLIs). Recordings were obtained from two groups of cells: MLIs with somata located in the proximal third of the molecular layer, within 25 μm of the Purkinje cell layer, which were considered as basket cells, and MLIs with somata in the distal two thirds of the molecular layer, which were considered as stellate cells. Slices were perfused (1.5 ml/min) with a saline containing (in mM): 125 NaCl, 2.5 KCl, 1.25 NaH_2PO_4, 26 $NaHCO_3$, 2 $CaCl_2$, 1 $MgCl_2$ and 10 glucose, equilibrated with a 95% O_2-5% CO_2 mixture (pH 7.3). Tight-seal whole-cell recordings (wcr) were performed with pipettes (5 to 8 MΩ) filled with a solution containing (in mM): 140 Kgluconate, 5.4 KCl, 4.1 $MgCl_2$, 9.9 HEPES-K, 0.36 Na-GTP and 3.6 Na-ATP. Oregon Green-BAPTA 1 (OG1; Molecular Probes, USA) was added at a concentration of either 20 or 100 μM. To determine the K_D of OG1 for Ca^{2+}, we performed *in vitro* calibration using the same intracellular solution (with 20 μM OG1) adjusted to Ca^{2+}concentration values ranging from 0 to 1.35 μM with concentrated K_2-EGTA and Ca^{2+}-EGTA stocks from the Ca^{2+} calibration buffer concentrate kit (C-3723; Molecular Probes, USA). The estimated K_D was 170 nM.

Data collection times ranged from 8 to 35 minutes after initiation of the wcr, for all experimental groups studied.

Fluorometric Ca_i imaging:

Fluorescence imaging was done in two different set-ups. Firstly, a digital imaging system from T.I.L.L. Photonics (Germany) consisting of a scanning monochromator (wavelength for the present study set at 488 nm) and a cooled

CCD camera (IMAGO QE; 1376 by 1040 pixels; pixel size: 204 nm after 63X magnification and 2 by 2 binning). Secondly, a home-made two-photon fast laser scanning system based on the design of Tan et al. (1999), with some modifications. Briefly, two-photon excitation was performed with a Ti-Sapphire laser (MaiTai, Spectra Physics, Mountain View, CA, USA) set at an excitation wavelength of 820 nm; average power at the specimen plane was kept between 6 and 10 mW. Axonal sub-regions were scanned by displacing the laser beam in the x-y direction with two galvanometers, using scanning and signal acquisition procedures as described (Tan et al., 1999). The effective pixel size was set at 250 nm. The emitted light was focused on the active surface of a photon counting avalanche photodiode (SPCM-AQR-13, PerkinElmer Optoelectronics, Canada) and sampled at 10 μs/point as detailed in Tan et al. (1999). The pseudocolor range for fluorescence images obtained through this detector are reported in Hz, calculated from the number of photons acquired during the 10 μs sampling interval. For most experiments, images were acquired with a dwell time of 50 to 100 ms/image in both, the digital imaging system and the 2-photon system. Faster frame rates (10 ms/image) were used in a sub-set of experiments carried out to determine the rise time of Ca_i transients. Both systems used upright Zeiss microscopes equipped with a 63X water immersion lens (numerical aperture: 0.9).

To induce axonal Ca_i rises, trains of action potentials (APs; 2 or 4 APs at 20 ms intervals) were produced by depolarizing the cell for 3 ms to 0 mV from a holding value of -70 mV (Tan and Llano, 1999). Analysis was performed by calculating the average fluorescence in "regions of interest" (ROI) as a function of time. The size of the ROIs was chosen as to just enclose the entire bouton and ranged from 1.5 to 4.5 μm^2. Values are

expressed as the percentage change in fluorescence with respect to control, $\Delta F/Fo = 100*(F-Fo)/(Fo-B)$, where F is the measured fluorescence signal at any given time, Fo the average from the pre-stimulus period, and B the average value, at each time point, of the background fluorescence from 4 regions of the imaged field which do not contain any part of the dye-filled cell.

Collection and statistical analysis of ROIs kinetic data

In each experiment, an axonal zone containing several hot spots was examined. Data were typically collected from 2 to 6 ROIs in each zone. The signal-to-noise ratio for individual ROIs was often improved by averaging over 2 to 4 trials, spaced at 1 minute intervals. The resulting average $\Delta F/Fo$ signal as a function of time was then fitted by single and double exponential functions. The fit was considered biexponential if both of the following criteria applied: (i) the ratio of the 2 time constants (fast time constant :τf; slow time constant: τs) was > 3 and, (ii) the amplitude coefficients for the slow time constant (As) and for the fast time constant (Af) were such that As/(As+Af) fell between 0.15 and 0.85. Peak $\Delta F/Fo$ amplitudes were calculated as the sum of the two amplitude coefficients for ROIs described by a double exponential decay. If one of the above criteria (or both of them) was not fulfilled, the kinetics were considered monoexponential, and the peak $\Delta F/Fo$ amplitude was the amplitude coefficient of the single exponential fit. After fitting the Ca_i decay, amplitude and kinetic parameters were averaged over the various ROIs belonging to one cell. Finally, results from different cells were pooled together to yield the mean values reported. Statistical variations in the text always refer to cell-to-cell variations; values of n refer to the number of cells, not of ROIs. These values are given as mean±s.e.m. To assess the statistical significance of decay time between different experimental conditions, an ANOVA test was performed in

order to control for multiple comparisons. Student's t-tests were used to identify significant differences among pairs; p values < 0.05 were considered significant.

Formulation of the functional equation system:

Each reaction depicted in Table 1 was described by two differential equations according to the law of mass action. In the present simulations, the Runge-Kutta of the fifth order method was used to solve the differential equations. Numerical simulations were performed with routines written in the IGOR Pro environment (Wavemetrix, OG, USA). To simulate a 4 AP stimulation, 4 successive instantaneous Ca^{2+} increases were introduced in the model, at 20 ms intervals. The magnitude of the Ca^{2+} load was adjusted at 11 μM/AP to approach the experimentally measured peak ΔF/Fo of PV(-/-) data, and then kept constant. A similar value of 12 μM/AP was found in the calyx of Held by Helmchen et al., 1997. Altering the Ca^{2+} load in the range 6 to 15 μM did not change appreciably the kinetics of the simulated decay (not shown).

Exchange out and into the compartment under consideration:

The single compartment under study (varicosity) exchanges Ca^{2+} with other cell compartments, as well as with the extracellular medium, using various processes operating on a time scale of tens of ms to seconds. As a first approximation, extrusion processes can be represented collectively by a Ca^{2+} flux that is proportional to the difference between the equilibrium Ca_i value (taken as 40 nM) and the current Ca_i value (Lee et al., 2000). This can be modeled by the simple kinetic reaction:

$$Ca \underset{k_{-1}}{\overset{k_1}{\rightleftarrows}} Ca$$

Here Ca on the left side of the reaction represents intracellular Ca^{2+}, and Ca on the right

side of the reaction represents extracellular Ca^{2+}. This scheme translates into

$d[Ca]_i/dt = - k_1[Ca]_i + k_{-1}[Ca]_e$

where $[Ca]_i$ and $[Ca]_e$ represent respectively the intracellular and extracellular Ca^{2+} concentrations and k_1 and k_{-1} represent the rate constants of Ca^{2+} extrusion and influx. $[Ca]_e$ is constant at a value of 2 mM. Note that k_1 corresponds to the extrusion rate γ of Lee et al. (2000). In the simulations k_1 was first determined on the basis of decay kinetics. k_{-1} was then calculated as $=k_1/50000$, such that the equilibrium value of Ca_i remained at 40 nM. Simulations are displayed in terms of $\Delta F/Fo$ for comparison with experimental results.

Diffusion equilibration :

MLI axons display a succession of "hot spots", where voltage-gated Ca^{2+} entry occurs, and passive regions. Hot spots correspond mainly to varicosities and are spaced approximately 5 μm apart (Forti et al., 2000). The time course of equilibration between dendritic spines and dendritic shaft in CA1 pyramidal cells was measured as 140 ms (Majewska et al., 2000), close to the value of τf in the present study. Since dendritic spines have roughly the same size as varicosities, it seemed possible that the fast component of decay could be contaminated by diffusion equilibration. If this were the case however, one would have expected to observe a fast component both in the WT and in the PV(-/-) strains, whereas in the latter case, the percentage of cells showing the fast component was significantly reduced. Thus the fast component of biexponential decays is not primarily due to diffusion. Nevertheless, it appeared possible that diffusion out of the varicosities could have distorted the results, particularly in the younger age group, since it has been shown that the separation between varicosities and linking axon segments

becomes more apparent with age (Forti et al., 2000; compare in the present work Fig. 1A1-B2 and 1C1-C2). To address this issue, we compared the analysis of the decay kinetics of the signal performed on small ROIs, as illustrated in Fig. 1, and on one very large ROI encompassing the entire frame (and hence, including several calcium hot spots and intervening "cold" axon). This analysis was performed on basket cell signals from PN10-12 WT mice. It was found that the decay required a biexponential fit independently of whether small or large ROIs were used, confirming that exit from the hot spots is not the main reason for biexponential decay time courses. Furthermore, quantitative differences between the results of the two analyses were modest. The largest difference concerned τf which was 25% larger with the large ROI than with the small ones (respective means, 0.23±0.02 s and 0.18±0.01 s); however, even this difference did not reach statistical significance at the $P<0.05$ confidence level. These results indicate that errors linked to the diffusion out of the varicosities are small, and justify our treatment with a one-compartment model.

Recording and analysis of IPSCs:

MLIs were maintained under voltage-clamp in the whole-cell recording configuration at a holding potential of –70 mV. The intracellular solution contained (in mM): 150 KCl, 2.4 $MgCl_2$, 10 HEPES-K, 1 mM EGTA-K, 0.4 Na-GTP, 2.4 Na-ATP (pH 7.3). Series resistance values ranged from 15 to 25 MΩ and were compensated for by 60%. Currents were filtered at 1.3 kHz and sampled at a rate of 250 μs/point. DL-2-amino-5-phosphonopentanoic acid (APV) and 6,7-Dinitroquinoxaline-2,3-dione (DNQX), antagonists of ionotropic glutamate receptors, were included in the bath solution at concentrations of 50 and 5 μM respectively. Extracellular stimulation of pre-synaptic axons was performed by applying voltage pulses (100 to 200 μs duration; 40 to 70 V

amplitude) between a reference platinum electrode and a pipette filled with a solution containing (in mM): 145 NaCl, 2.5 KCl, 2 $CaCl_2$, 1 $MgCl_2$, 10 HEPES; input resistance of 2 to 3 MΩ). This pipette was displaced in the molecular layer until a stable synaptic response was evoked. The standard experimental protocol consisted of acquiring 1 sec of baseline currents followed by the application of a 50 Hz train of 10 stimulus. This protocol was repeated 10 to 20 times, at 10 to 20 s intervals. Detection and analysis of IPSCs were performed off-line with routines written in the IGOR-Pro programming environment. Results are reported in terms of the frequency of synaptic events as a function of time, relative to the pre-stimulus period.

Immunocytochemistry:

Immunocytochemistry was performed on C57 Black 6 mice from PN10 to PN38. Animals were anesthetized by an intraperitoneal injection of 150 µl Pentobarbital (Sanofi) diluted 5x in a 0.9 % NaCl solution and transcardialy perfused with a cold (5-6°C) 0.9 % NaCl solution, followed by a cold fixative solution consisting of 4 % paraformaldehyde, 0.2 % glutaraldehyde and 0.2 % picric acid in 0.15 M phosphate buffer at pH 7.4. After 20 minutes, the cerebellar vermis was removed and post-fixed overnight in the same fixative solution, excluding glutaraldehyde. Sagittal cerebellar slices (50 µm thick) were cut after 24 hours fixation in cold 0.15 M phosphate buffer with a vibratome (VT 1000S, Leica, Germany). All incubations were performed under continuous agitation at room temperature in 24-well culture plates. The sections were thoroughly washed in PBS (Phosphate buffer 0.03 M with 0.9 % NaCl), then incubated 2 hours in PBS containing 0.2 % Triton for permeabilization; PBST) and 2 % bovine serum albumin (BSA, Sigma A 2153). Sections were incubated overnight with one or two of the following pairs of antibodies, prepared in PBST: (i) a polyclonal rabbit anti-parvalbumin (SWant PV-28,

1/1000) and a monoclonal mouse anti-calbindin D 28-K (SWant 300, 1/1000), (ii) a polyclonal rabbit anti-calbindin (SWant CB-38, 1/1000) and a monoclonal mouse anti-GABA (SWant 3A12, 1/1000). After several washes with PBST, slices were incubated in the dark for 2 hours in one of the following pairs of secondary antibodies, both prepared in PBST: (i) fluorescein anti-rabbit IgG (Vector FI-1000, 1/200) and Texas-red anti-mouse IgG (Vector TI-2000, 1/200), (ii) CY3 anti-rabbit IgG (Jackson Immunoresearch 111-165-144, 1/300) and Alexa 488 anti-mouse IgG (Molecular Probes A-11001, 1/300). After several washes with PBS, slices were mounted on glass slides in Prolong Anti-fade kit mounting medium (Molecular Probes P 7481).

A first control consisted in incubations without the primary antibodies and with the two secondary antibodies; no specific signal was detected. The second control was to omit one of the two primary antibodies from the incubation medium maintaining the two secondary antibodies. The signal was positive for the primary antibody which remained and had the same pattern as that observed in double immunostaining.

Confocal images were acquired with a Zeiss LSM 510 confocal microscope equipped with two lasers, Argon multiray (used at 488 nm) and Helium (543 nm). Sections were analyzed using a 40X oil-immersion objective with a numerical aperture of 1.3. The pin hole aperture and the laser power were respectively 74 µm and 8 % for the Argon laser, 65 µm and 30 % for the Helium laser.

Biochemistry:

Mice (PN5 to PN25 and young adults; n = 3 for each age group) were deeply anesthetized by inhalation of CO_2 and briefly perfused transcardialy by ice-cold phosphate-buffered saline solution (PBS). Cerebella were dissected and homogenized in 10 mM Tris-HCl, 1 mM EDTA, pH 7.4 (containing 1 tablet of protease inhibitor cocktail

(Roche Diagnostics AG, Rotkreuz, Switzerland) per 10 ml of buffer, added just prior to use) using a Polytron homogenizer. Soluble protein fractions were prepared by centrifugation of homogenates at 30,000g for 30 minutes and recovering the supernatant. Proteins (25 µg) were separated by one-dimensional polyacrylamide gel electrophoresis (15%) and transferred on nitrocellulose membranes using a semi-dry transfer system (Bio-Rad, Laboratories, Glattbrugg, Switzerland). The membranes were controlled for even load and possible transfer artifacts by staining with Ponceau red solution. After blocking with 10% solution of nonfat milk in TBS-T buffer (TBS with addition of 0.05% of Tween 20), membranes were incubated with primary antibodies against PV (PV28, 1: 1000 SWant Bellinzona, Switzerland) for 90 min. All antibodies used were dissolved in TBS-T solution containing 1 % of protease-free BSA. Incubation of membranes with primary antibodies was followed by extensive washing using TBS-T solution and subsequently by incubation of membranes with anti-rabbit secondary biotinylated antibodies (Vector Laboratories, Burlingame, CA, 1:10000). After extensive washing, membrane were incubated with avidin-biotin conjugated peroxidase (Vector Laboratories) solution in TBS-T and washed again. The bands corresponding to PV were visualized and quantified by the Molecular Imager (Bio-Rad) using the ECL chemiluminescence method (Pierce, Perbio Science SA, Lausanne, Switzerland).

Results

Decay kinetics of axonal Ca_i signals are different in basket cells and stellate cells at early developmental stages

Interneurons of the molecular layer of the cerebellum (MLIs) are traditionally classified as basket and stellate cells. The former neurons have cell bodies in the lower

third of the molecular layer and make extensive synaptic contacts with Purkinje cell somata whereas the latter ones have cell bodies in the upper two thirds of the molecular layer and innervate preferentially Purkinje cells dendrites. The two classes of neurons are closely related and are sometimes considered as a continuum (Sultan and Bower, 1998). No functional difference has been revealed so far between them, except for the fact that the current evoked in Purkinje cells is larger for presynaptic basket cells than for presynaptic stellate cells (Vincent and Marty, 1996). However, we found that at PN10-12, there was a striking difference between MLIs with somata located within 25 μm of the Purkinje cell layer (hereon called basket cells) and MLIs whose somata were placed in the upper two thirds of the molecular layer (hereon called stellate cells) concerning the time course of decay of Ca_i transients. Figures 1A and B illustrate the action potential (AP)-evoked fluorescence changes reported by OG1 (100 μM) in axons of PN10-12 MLIs. Fluorescence signals were collected at small hot spots which represent putative release sites onto Purkinje cells and onto other MLIs (Llano et al., 1997; Tan and Llano, 1999; Forti et al., 2000). Analysis was performed in terms of the percentage change in fluorescence over the baseline period ($\Delta F/Fo$) in small regions of interest (ROIs) whose size was set to just encompass the entire bouton (see Methods). Following a 50 Hz train of 4 APs, $\Delta F/Fo$ increases of 100-150 % were measured, corresponding to over 2-fold Ca_i rises. The fluorescence signals decayed back to baseline within a few seconds. The decay was much faster in basket cells than in stellate cells. This functional difference is exemplified in Figures 1A and 1B, where 2 photon fluorescence images corresponding to scans of axonal regions at rest and at the peak of the response to the stimulus are displayed, along with the time course at selected ROIs. On average, the time of decay to half of peak amplitude (50% decay) was 4-fold slower for stellate than for basket cells

(0.813±0.09 s, n= 7 cells and 0.202±0.02 s, n= 6 cells, respectively), a highly significant difference (Student's t-test $p<0.00018$; pooled data in Fig. 1D). Furthermore, whereas a large fraction of the stellate cell signals could be well approximated by a single exponential function (examples in Fig. 1A3), data for basket cells (examples in Fig. 1B3) were much better fitted by a double exponential (red traces) than by a single exponential (blue traces). Using the criteria explained in Methods, we found that decay kinetics were monoexponential in 49±18 % of the signals from of PN10-12 stellate cells (average τ: 1.45±0.21 s; n=7 cells) whereas a double exponential was required to describe Ca_i transients in 89±7 % of PN10-12 basket cells (τf: 0.18±0.01 s, τs: 1.86±0.48 s, As/(Af+As): 0.29±0.06; n=5 cells). Thus the kinetic difference between stellate and basket cell signals involved not only a difference in overall speed, but also in the very shape of the decay.

Age-dependent changes in the temporal dynamics of axonal Ca_i signals in cerebellar interneurons

We next explored whether Ca_i decay kinetics changed differentially for basket and stellate cells during development. To quantify the effects, two age groups were considered; they covered the ages PN10-12 and PN19-21. Basket cell Ca_i signals changed little between the two age groups which were examined (at PN19-21, 50% decay time : 0.168±0.03 s; biexponential fits required for 90±10 % of the transients; τf: 0.140±0.02 s, τs: 1.38±0.46 s, As/(Af+As): 0.33±0.05; n=5 cells). In contrast, the 50% decay time for stellate cells was approximately 4 times shorter at PN19-21 (0.234±0.02, n=6 cells) than at PN10-12, a highly significant change (Student's t test comparison of PN10-12 and PN19-21 stellate cells: $p<0.0002$). As a result of this remarkable change with age, at PN19-21 there was no significant distinction between the decay time course of the two interneuron subtypes (see summary results for 50% decay in Fig. 1D). Furthermore, all the stellate cells in

the PN19-21 group had a biexponential time course (τf: 0.176±0.02 s, τs: 1.83±0.22 s, As/(Af+As): 0.39±0.03; n=6 cells; examples in Fig. 1C) similar to that describing the decay of PN10-12 and PN19-21 basket cells.

The expression of PV in the developing cerebellum

Ca_i kinetics are shaped by a complex interaction between extrusion mechanisms, exchange with intracellular Ca^{2+} stores (reviewed by Pozzan et al., 1994; Berridge, 1998), diffusion (Majewska et al., 2000) and endogenous Ca^{2+} buffers (Neher and Augustine, 1992). In several systems, the contribution of these processes to the decay of Ca_i transients has been inferred from the relative goodness of fit by either a mono- or a bi-exponential function. Monophasic decays were attributed to linear Ca^{2+} extrusion mechanisms and rapid kinetics of Ca^{2+} buffers (Lee et al., 2000). Biphasic decay kinetics have been interpreted in terms of different mechanisms including non linear Ca^{2+} extrusion (Fierro et al., 1998), saturation of high affinity CBPs such as CB (Maeda et al., 1999; Blatow et al., 2003), or delayed buffering by PV (Lee et al., 2000). Since MLIs express neither CR nor CB, but are known to be rich in PV (Kosaka et al., 1993), we next examined whether a correlation exists between PV expression levels and kinetics of presynaptic Ca_i transients.

In the cerebellar molecular layer, PV is present not only in MLIs but also in Purkinje cells. The extensive dendritic arborization of Purkinje cells hinders the visualization of the small MLI somata when slices are stained with antibodies for PV. We therefore performed double stainings with antibodies for PV and CB, as shown by the confocal images presented in Fig. 2A. Due to the choice of secondary antibodies (see Methods), cells containing both CBPs (Purkinje cells) appear yellow-orange and MLIs,

which express only PV, appear green. At PN10 (Fig. 2A1), the distribution of PV was clearly heterogeneous in the molecular layer, with a much lower staining in the outer part, corresponding to stellate cells, than in the inner part, corresponding to basket cells (see below). These data suggest that the difference between the decay kinetics of basket and stellate cells observed at this age is directly determined by the level of PV expression: the low PV-expressing stellate cells have a decay that is primarily determined by clearance of Ca^{2+}, and which is therefore monoexponential according to the predictions of the simple "one compartment model" (Neher, 1998), whereas for basket cells, Ca^{2+}-binding to PV accelerates the initial part of the Ca_i decay, producing a biexponential time course.

During development, there was a marked general increase in the level of PV expression, as determined by quantitative Western blots from cerebellar slices (Fig. 2B). PV was just detectable at PN5. Between PN10 and PN20, the increase was approximately 5-fold. Counts of the number of PV-positive interneurons from PV/CB stains of slices in the same age window were in agreement with this developmental trend (example of staining at PN20 in Fig. 2A2; quantitative analysis at different ages in Fig. 2A3). Furthermore, the pattern of PV expression throughout the molecular layer evolved with age, such that at early ages most PV-positive MLIs were located close to the PC layer and with increased age PV-positive MLIs started to appear farther into the molecular layer (Fig. 2A4). To quantify the density of MLIs in the two age groups studied, we performed double stainings with antibodies for GABA and CB. Examples of this type of stain are shown in Fig. 2C1 (at PN12) and Fig. 2C2 (at PN20). Here, cells containing GABA and CB appear red-orange (prominent staining in Purkinje cells), whereas MLIs appear green (GABA-positive, CB-negative). The analysis of this type of staining showed that the

density of GABA-positive MLIs was not significantly different between PN12 and PN20, whereas the density of PV positive MLIs increases between the two developmental stages (Fig. 2C3).

MLIs derive postnatally from precursors near the IVth ventricle that migrate through the white matter to the cerebellar cortex (Zhang and Goldman, 1996). Basket cells settle down first in the lower part of the molecular layer. As the depth of this layer increases, stellate cells gradually move in to fill more distal locations. Thus at PN10-12, corresponding to the final phase of the build-up of the molecular layer, basket cells have been occupying their location for some time, whereas stellate cells are new comers. The results of Fig. 2 suggest that MLIs have little PV at first, but that they acquire PV a few days after settling down in the molecular layer.

In addition, these results parallel the above finding that the decay time course of stellate cells changes much more dramatically than that of basket cells with age, and they account for the nature of the kinetic change, which converts a monophasic, low-PV decay to a biphasic, high-PV decay. Taken together, the results indicate a strong correlation between the level of PV expression and the degree of biphasicity of the Ca_i decay.

Ca_i signaling in axons from PV(-/-) mice

If the above reasoning and conclusions are correct, eliminating PV expression by genetic deletion of a functional PV gene should have little effect in stellate cells from PN10-12 mice, but it should convert the biphasic decay of PN10-12 basket cells and that of both types of interneurons at PN19-21 into a slower, monophasic decay similar to that measured in WT stellate cells at PN10-12. To test these predictions, decay kinetics were analyzed in a PV null-mutant, PV(-/-) mouse strain (Schwaller et al., 1999) and compared to age-matched controls. The two PN10-12 groups were differently affected by PV-

deficiency. There was no change in kinetics for stellate cells (50% decay: 0.977±0.13 s, Student's t test $p<0.37$; monophasic decay for 50±28% of the signals, Student's t test $p<0.97$; n= 3 cells). For basket cells, on the other hand, lack of PV led to a marked slowing of the decay (50% decay: 0.618±0.02, Student's t test $p<0.00002$), which was described by a single exponential in 83±16% of the signals (Student's t test $p<0.002$; n=3 cells). A representative example of the AP-evoked Ca_i transients obtained in axonal varicosities of a PV(-/-) PN12 basket cell is shown in Fig. 3A. For PN19-21 PV(-/-) mice, the decay of Ca_i signals was much slower than that observed in MLIs from age-matched WT animals. Statistical comparisons were performed by pooling data from basket and stellate cells together, since at this age the two cell types display similar decay kinetics, both in the WT and in PV(-/-) strain. Average 50% decay values in PN19-21 PV(-/-) mice were 0.62±0.12 s (n=10 cells), 3-fold higher than controls (pooled average from age-matched controls: 0.203±0.019 s, n = 11 cells; Student's t test $p<0.003$). The difference applies as well to the shape of the decay, which was well described by a single exponential for 66±10 % of the signals in PV(-/-) mice (average τ: 0.93±0.18 s; n=10 cells), whereas in WT MLIs at this age, a double exponential was required to describe Ca_i decay kinetics for 95.5±4.5% of the signals (n=11 cells; Student's t test $p<0.00016$). These results, summarized in Fig. 3B, show that the absence of PV essentially maintains PN19-21 interneurons at PN10-12 stellate cell kinetics, thus matching exactly the above predictions and strongly reinforcing our conclusion that PV is the major determinant in shaping the biphasic decay kinetics in MLI axons.

Finally peak amplitudes were compared in WT and in PV(-/-) mice. Since PV has slow binding kinetics with Ca^{2+}, the presence of PV is expected to have little influence on the peak amplitude and rise time of Ca_i transients (Lee et al., 2000; Schmidt et al.,

2003a). In accord with this prediction, peak ΔF/Fo values in PN19-21 PV(-/-) mice (147±11 %, 10 cells) were not significantly different from those obtained in age-matched WT (109±14 %, 11 cells; Student's t test $p<0.06$). Furthermore, times from stimulus onset to peak for trains of 4 APs, analyzed in a sub-set of experiments performed with sampling rates of 10 ms per image, were similar in both groups (WT : 81.9±1.9 ms; PV(-/-) : 99.1±21.9 ms; n=3 cells per group; Student's t test $p<0.48$).

When comparing Ca_i signals at different ages and PV conditions, the question arises as to the possible differences on the wash-out of cytosolic components amongst the experimental groups. As mentioned in Methods, data was gathered at wcr times ranging from 8 to 35 min in all experimental groups. Neither peak amplitudes nor decay time course, including the degree of biphasicity and τ values of the Ca_i decay in MLIs from WT mice showed any correlation with wcr time. We therefore conclude that PV does not readily diffuse out of MLIs axons within the time window of the present experiments.

Modeling AP-evoked presynaptic Ca_i transients

We simulated volume averaged Ca_i for different experimental conditions in order to (i) estimate the endogenous PV concentration and (ii) predict the actual shape of Ca_i decay in the absence of exogenous buffer (i.e., Ca^{2+} indicator). These simulations were based on the "one compartment approximation" as developed in chromaffin cells, which assumes a homogeneous Ca^{2+} concentration in the compartment (Neher and Augustine, 1992). The simulations obeyed a system of differential equations describing (i) the reactions of Ca^{2+} with its various binding partners (OG1, PV and ATP), (ii) the reaction of Mg^{2+} with PV and ATP and (iii) an exchange of the compartment with other cell compartments and with the extracellular medium, based on a simple reaction with

Ca^{2+}-independent rate constants (see Methods and Table 1 for reaction parameters). Additionally an endogenous fast buffer was included, following the evidence presented below.

Evidence indicating the presence of an endogenous buffer distinct from PV:

Besides PV, MLIs may contain some fast endogenous buffer which could be up or down regulated during development, and which could affect the kinetics of Ca_i decay. Dissecting individual buffer contributions in a cell containing PV plus one (or more) fast buffers is complicated and can easily lead to erroneous conclusions (see review by Markram et al., 1998). PV(-/-) conditions are more advantageous, since the absence of slow buffer greatly simplifies the system of equations describing Ca_i decay. In this situation, the strength of the endogenous buffer can be estimated by extrapolating the linear relation between τ and probe concentration (Neher and Augustine, 1992; Lee et al., 2000):

$$\tau = (1 + \kappa_S + \kappa_B)/ \gamma \quad (1)$$

where κ_S and κ_B respectively represent the buffering capacity of the endogenous fast buffer and of the dye, and γ the rate constant representing extrusion from the compartment. We used the predictions of eq. (1) to assess the presence of a fast buffer in MLIs. We reexamined PV(-/-) data both in PN10-12 and in PN19-21 animals, using a much lower concentration of OG1 (20 μM instead of 100 μM). Even with the low dye concentration, good quality signals could be collected, as illustrated in Fig. 4A for a PN19 PV(-/-) stellate cell. The AP-evoked Ca_i transients were well described by a single exponential in all cells tested (example in Fig. 4A3), with τ values of 1.02±0.10 s (4 cells) at PN10-P12 and 0.47±0.15 s (4 cells) at PN19-21. Corresponding average peak $\Delta F/Fo$

were 146±18 % at PN10-12 and 204±28% at PN19-21. Using eq. (1) κ_s was calculated for the two age groups. Values were 1170 and 350 for PN10-12 and PN19-21 MLIs, respectively. Thus, the analysis of PV (-/-) data indicates that MLIs contain a substantial amount of a fast endogenous buffer, with a buffering capacity that declines with age.

We next proceeded to simulate the Ca_i transients for the PV (-/-) data, focusing on the PN19-21 group. Fig. 4B shows the results of the first set of simulations, aimed at determining (i) the magnitude of the Ca^{2+} load and (ii) the kinetic parameters for the extrusion from the compartment. Averaged experimental results from the PV(-/-) PN19-21 group for 20 μM (black trace) and 100 μM OG1 (blue trace) are displayed along with the best approximations to the data (red and yellow traces, for 20 and 100 μM OG1, respectively). The simulations, which include an endogenous buffer with a κ_s of 350 (i. e., equivalent to 60 μM OG1), yield a Ca^{2+} load of 11 μM per AP, and extrusion/influx kinetic constants k_1 and k_{-1} of 550 s^{-1} and 0.011 s^{-1}, respectively. In the absence of endogenous buffer, the predicted time course for 20 μM OG1 (green trace) is much faster than the experimental data (continuous black trace) in accord with the presence of a substantial fast endogenous buffer.

Modeling the effects of PV on Ca_i decay

Using the parameters which best approximated PV(-/-) PN19-21 results, we set out to determine the concentration of PV in axons of WT MLIs. For this, we compared numerical simulations with the average experimental data obtained with 100 μM OG1. As shown by the family of curves in Fig. 5A and in accord with previous publications (Lee et al., 2000; Schmidt et al., 2003a; reviewed by Schwaller et al., 2002), the decay kinetics in the presence of PV are described by a double exponential. Changes in PV concentration had little effect on the peak ΔF/Fo value but altered markedly the kinetics

of the Ca_i decay. With increasing PV concentration, the fast time constant of the decay became faster, while the slow time constant of the decay slowed down (not shown; Lee et al., 2000). However, independently of the PV concentration, these simulations differed significantly from the experimental results, represented by the black trace in Fig. 5A. An acceptable approximation to the WT PN19-21 data could only be achieved by increasing the extrusion rate constants 2-fold. This is shown in Fig. 5B, where a PV concentration of 150 μM yields the best approximation to the parameters extracted from WT PN19-P21 MLIs subjected to 4AP trains, including peak ΔF/Fo, τf and τs, as well as ratio of the corresponding amplitude coefficients (average values from 11 MLIs were, peak ΔF/Fo: 109.5±14.6 %, τf: 0.16±0.01 s, τs: 1.63±0.23 s, As/(Af+As): 0.36±0.03).

It is important to stress here that changing the extrusion rate from the PV (-/-) simulation was the only satisfactory solution to remove the discrepancy shown in Fig. 5A. In particular, changing the value of κ_s (the buffering capacity of the fast endogenous buffer) between WT and PV(-/-) was unable to produce a satisfactory fit. Likewise, even if the affinity and binding rates of OG1 for Ca^{2+} were artificially modified, no single set of parameters could account for WT and PV(-/-) data without altering the exit rate between the two conditions (not shown). A compensatory change in the extrusion rate was found previously upon deletion of CB in Purkinje cells (Eilers et al., 2003).

All simulations so far assume a resting Ca_i level of 40 nM, both for WT and PV(-/-) conditions. Reported neuronal basal Ca_i values range from 20 nM (Fierro and Llano, 1996) to 70 nM (Jackson and Redman, 2003). Satisfactory sets of simulations could be obtained with different resting Ca_i values, provided that the model parameters were readjusted; thus the best PV concentration was 175 μM for a resting Ca_i level of 20 nM,

and 120 μM for a resting Ca_i level of 70 nM.

Does PV saturate during bursts of AP firing?

PV is a high affinity buffer, which is partially Ca^{2+}-bound at resting Ca_i levels. In chromaffin cells which were infused with PV, repetitive stimulation was shown to increase the degree of saturation of PV, leading to supralinear Ca_i increases and to slower decay kinetics (Lee et al., 2000). In the present case the calculated apparent dissociation constant (based on parameters listed on Table I) of PV for Ca^{2+} was rather high (450 nM) due to the comparatively large concentration of Mg^{2+} that was included in the pipette solution. Accordingly, only 8% of PV was bound to Ca^{2+} under resting conditions. The amount of free PV dropped by 10% of the resting value following one AP (calculated 20 ms after the AP), to 23% following a 3-AP train, and to 36 % following a 9-AP train (simulations not shown). Thus, it is predicted that the kinetics of PV binding to Ca^{2+} will be mildly altered with action potential number, at least for trains of a few action potentials.

This was tested experimentally. Results presented so far have been restricted to 4-AP trains at 20 ms intervals. This protocol was chosen because Ca_i signals had a good signal-to-noise ratio and gave reliable kinetic data. However results with shorter trains were also gathered in some experiments in order to explore the possible consequences of activity-driven PV saturation. Because τ_f is related to the PV concentration, as discussed above, we focused our attention on this parameter. In WT PN19-21 animals, average τ_f values were 0.14±0.03 s and 0.16±0.01 s for Ca_i rises evoked by 2 and 4 APs respectively (8 and 11 cells respectively; OG1: 100 μM). These results are in agreement with the above notion that PV is not saturated for short AP trains.

Simulation of the dye-free Ca_i transient

The preceding analysis gives an estimate of the PV concentration as well as the buffering capacity of the fast endogenous buffer, but does not allow to estimate separately the concentration and the affinity of this buffer. However, within the time scale pertaining to this work, knowledge of the buffering capacity is all that is needed to simulate the Ca_i time course dictated by the endogenous buffers, without the perturbation of added calcium indicator. Fig.6A shows the calculated decay of the Ca_i transient induced by the standard experimental protocol, i.e., a 50 Hz 4 AP train, as well as by a stronger stimulus (10 APs, 50 Hz). For both stimulation protocols, comparison of the WT (black traces in Fig. 6A) with the PV(-/-) prediction (red traces in Fig. 6A) illustrates the dramatic impact of PV on Ca_i decay. In the absence of PV Ca_i has returned close to baseline levels 1 sec after reaching its peak. In contrast, when PV is present, a long-lasting tail characterizes the Ca_i decay. Actual PV effects could be even larger, for two reasons. First, the Mg^{2+} concentration that was chosen for our intracellular solution (660 μM) is at the upper limit of likely physiological values; any lower Mg^{2+} concentration would increase the apparent affinity for Ca^{2+} and thus increase PV's efficacy to bind Ca^{2+}, prolonging the slow decay. Secondly, it cannot be excluded that some washout of PV occurred during our experiments. For these two reasons, the biphasic pattern of WT Ca_i decay is, if anything, even more marked than is apparent in Fig. 6A.

PV enhances delayed transmitter release:

When MLIs discharge in short bursts at 10-50 Hz, as they do under resting conditions *in vivo* (Eccles et al., 1966; Ekerot and Jörntell, 2001), little summation is

expected for the fast component of Ca_i decay, because of a lack of synchronization. The amplitude of the slow decay component, however, increases with the number of spikes. Note the contrast in Fig. 6A between the dashed black trace, reflecting the Ca_i decay following 10 APs, with the continuous black trace, simulating 4-AP train data. By comparison, residual Ca_i decay in PV(-/-) conditions is short and almost independent of AP number (dashed and continuous red traces in Fig. 6A). Since bursts of up to 10 APs have been observed in MLIs following parallel fiber stimulation *in vivo* (Eccles et al., 1966), the question arises as to whether the slow return of the presynaptic Ca_i elevation predicted by the model could induce a measurable increase in transmitter release.

To test these predictions, gabaergic synaptic currents were studied in response to trains of presynaptic stimulations (10 stimuli at 50 Hz) in WT and PV(-/-) mice. Experiments were performed on PN19-21 mice to ensure the presence of PV in all presynaptic fibers of the WT group. As observed earlier at other gabaergic synapses (Lu and Trussell, 2000; Kirischuk and Grantyn, 2003), asynchronous release was apparent during the train, with a frequency that increased with stimulus number (Fig. 6B2, B4 where vertical arrows point to asynchronous events). However, there was no significant difference between WT and PV(-/-) data concerning asynchronous release frequencies (WT: 10 ± 4 Hz after the 1st stimulus, and 29 ± 5 Hz after the 10th stimulus; PV(-/-): 8 ± 2 Hz after the 1st stimulus, and 25 ± 4 Hz after the 10th stimulus). Delayed transmitter release (Kirischuk and Grantyn, 2003) was apparent both in the WT (Fig. 6B1) and in the PV(-/-) groups (Fig. 6B3). Here, striking kinetic differences appeared between the two groups. In WT, delayed release extended up to 2400 ms after the train (Fig. 6C1), whereas in PV(-/-) mice, significant delayed release stopped 400 ms following the end of the train (Fig. 6C2). Furthermore we found that both in the WT and in PV(-/-), the Ca_i decay

predicted from the model (blue curves in Fig. 6C1-C2) superimposed with WT and PV(-/-) data after appropriate scaling. The required scaling factors were in a ratio of 1.5, indicating that in PV(-/-), a given Ca_i signal was 1.5-times less efficient than in WT in eliciting delayed release. This may be related to the fact that the synapse is depressing in WT but facilitating in PV(-/-) (Caillard et al., 2000; likewise in the present experiments, the amplitude ratio of the 10th IPSC over the first was on average 0.76 in WT and 1.11 in PV(-/-)). We conclude that delayed release is prominent in MLI-MLI synapses, and that the presence of PV in the presynaptic terminals markedly prolongs its time course.

Discussion

The presence of PV governs Ca_i decay kinetics:

We found 3 situations where the presence of PV determined the shape of the Ca_i decay. (i) At PN10-12 PV was present only in basket cells. At this age basket cells had biphasic Ca_i decay, whereas stellate cells mainly displayed a monoexponential decay. (ii) PV was present in stellate cells at PN19-21 but not at PN10-12. We found that the Ca_i decay of stellate cells was converted from monoexponential to biexponential over the same time period. (iii) Finally, WT and PV(-/-) results were compared for PN10-12 basket cells and for PN19-21 MLIs. In both cases removal of PV converted a biexponential decay into a monoexponential one. From these results we conclude that the presence of PV in MLI terminals determines a specific kinetic signature for Ca_i decay, characterized by a biexponential time course. This change is accompanied by a marked acceleration of the first part of the decay.

In spite of this, a fraction of the decays required a biexponential fit under conditions where the PV concentration was small or null: in stellate cells from young WT animals, as well as in MLIs from mature PV(-/-) mice. As discussed elsewhere (Koester

and Sakmann, 2000), non-linear clearance systems and/or deviations from the assumptions of the single compartment model are likely explanations for these findings.

Ca$_i$ decay and intrinsic calcium buffering capacity in gabaergic vs. glutamatergic terminals:

Using the "single compartment approximation" (Neher, 1998) and procedures developed in chromaffin cells (Neher and Augustine, 1992) estimates have been obtained for κ_S at various glutamatergic terminals. Results range from 19 (Jackson and Redman, 2003) to 140 (Koester and Sakmann, 2000) while the extrapolated dye-free decay time constant ranges from 30 ms (CA1-CA3 boutons: Sinha et al., 1997) to 100 ms (calyx of Held: Helmchen et al., 1997). From the present study it appears that the buffering capacity of PN19-21 terminals amounts to 670 (for PV) plus 350 (for the fast endogenous buffer), adding up to a total κ_S value of 1020. Therefore, MLI terminals have a buffering power comparable to that of Purkinje neurons (Fierro ad Llano, 1996), 1-2 orders of magnitude higher than that reported for glutamatergic terminals. Because many gabaergic interneurons are known to contain high concentrations of CBPs, this may reflect a basic difference between the functioning of gabaergic and glutamatergic synapses. In cerebellar MLIs, the endogenous fast buffer and PV exert opposite effects on the speed of the initial decay phase, so that the estimated dye-free decay time constant (39 ms) ends up similar to those calculated for glutamatergic terminals. Thus, the presence of PV may have evolved as a mean to combine the large buffering power common to many gabaergic neurons with the need to obtain a sufficiently fast initial Ca$_i$ decay. In addition, PV induces a prominent second component with a time constant of 0.6 s. Below, some of the functional consequences of the specific shape of Ca$_i$ decay of MLI terminals are envisaged. An additional, more practical consequence of the large

buffering power of gabaergic terminals is that perturbations linked to dye loading are expected to be much less severe in measurements taken from gabaergic than from glutamatergic terminals, making the analysis of presynaptic Ca_i signals easier.

PV and development:

Our results suggest that PV expression increases precisely at the time when MLIs stop migrating and start establishing functional synapses. The appearance of PV increases temporal separation between responses to consecutive Ca_i-raising stimuli by accelerating the initial slope of Ca_i decay. Furthermore, it may increase spatial separation between such stimuli, since buffering by PV may decrease the apparent diffusion constant of Ca^{2+}. By contrast, the fast buffer that is strongly expressed at PN10-12 slows Ca_i signals and (if it is readily diffusible) may promote their spread along the axon. Our PV(-/-) data suggests that the strength of this buffer declines as PV concentration increases. Thus, the replacement of the fast initial buffer by PV likely contributes to the transition from widespread and slow Ca_i signals used for trophic effects (cell migration and neurite outgrowth) to local and fast Ca_i signals used for synaptic transmission.

Physiological implications:

The implications of CBPs in cerebellar function has been previously assessed through the analysis of somato-dendritic Ca_i signaling and motor behavior in mice lacking the fast buffer CB (Airaksinen et al., 1997; Barski et al., 2003). In the present work, we focused on the presynaptic role of the slower buffer PV. As pointed out before (Neher, 1998), addition of Ca^{2+} buffers does not alter the integral of the Ca_i transient, but rather its kinetics. Therefore physiological effects are expected mainly on non linear or non integrating calcium sensors. For instance, in hair cells, the presence of high

concentrations of a fast endogenous buffer has long been proposed on experimental and theoretical grounds to regulate calcium dependent K^+ channels, and hence to influence the cell responses to fast sensory inputs (Roberts, 1993; 1994; Ricci et al., 1998). This buffer has recently been identified as calretinin in frog saccular hair cells (Edmonds et al., 2000). In the present case, several possible effects of adding or suppressing the slow Ca^{2+} buffer PV may be envisaged.

First, for doublet stimulations, the presence of PV insures a quick decay to a small amplitude slow component, so that facilitation and asynchronous release are both minimal. We found earlier that in WT animals, MLI-Purkinje cell synapses display no paired pulse facilitation (inter-pulse intervals: 30-100 ms), whereas these synapses display substantial paired pulse facilitation in PV(-/-) mice (Caillard et al., 2000). This study was performed in P7-12 MLIs; with retrospect it appears likely that most recordings were performed with basket cells, given the present finding of selective staining of these cells with a PV-directed antibody.

Secondly, the presence of PV slows down the late part of the Ca_i decay. We have shown that this effect leads to a prominent slow presynaptic residual Ca_i signal after a train of APs, and is then responsible for a very pronounced delayed release that lasts for seconds. Delayed release can be very prominent in gabaergic synapses following trains of 10 APs or more (Lu and Trussell, 2000; Kirischuk and Grantyn, 2003). Our results suggest that this property does not require a special molecular machinery responsible for exocytosis, but more simply, that it is due to a prolongation of Ca_i decay due to the presence of powerful Ca^{2+} buffers. They also suggest that PV is particularly effective in this respect because of its slow binding properties. It is important to stress that due to delayed release, a bursting MLI generates a significant synaptic signal even during

interburst intervals. Indeed, the integral of the delayed signal in the record illustrated in Fig. 6b2 is larger than that of the signal generated during the trains, which is limited by synaptic depression and by receptor saturation (Auger and Marty, 1997). It is therefore interesting to reflect on this unconventional mode of synapse operation. During the interburst period, the MLI gives a random, almost steady synaptic output, with a mean intensity that is primarily determined by the number of APs in the preceding burst. Thus, during bursting, MLIs (and possibly, many other PV-containing interneurons) adopt alternately a phasic signaling mode during the bursts and an integrating signaling mode between bursts.

Third, PV's Ca^{2+}binding kinetics together with its role on "buffered" diffusion as discussed above might affect intracellular Ca^{2+} release channels and could play an important role in shaping GABA release at the presynaptic terminals of MLIs. In Xenopus oocytes, it has been elegantly demonstrated that overexpression of PV can induce Ca^{2+} puffs, which were attributed to spontaneous Ca^{2+} release through inositol trisphosphate receptors (IP_3Rs) (John et al., 2001). More recently, in the same preparation, PV was shown to regulate the spatial distribution of IP_3R-mediated Ca^{2+} puffs (Dargan et al., 2004). No evidence is as yet available for the existence of functional IP_3Rs in MLIs. However, work from our laboratory has shown that ryanodine-sensitive Ca^{2+} stores are functional at their axonal terminals and that they produce highly localized spontaneous Ca_i transients (SCaTs) which contribute to neurotransmitter release (Llano et al., 2000). The spatial and temporal dynamics of these events will certainly be shaped by the rather high PV concentration at MLIs terminals predicted from the present work.

References

Airaksinen MS, Eilers J, Garaschuk O, Thoenen H, Konnerth A, Meyer, M (1997) Ataxia and altered dendritic calcium signaling in mice carrying a targeted null mutation of the calbindin D28k gene. Proc Ntl Acad Sci (USA) 94: 1488-1493.

Atluri PP, Regehr WG (1998) Delayed release of neurotransmitter from cerebellar granule cells. J Neurosci 18: 8214-8227.

Auger C, Marty A (1997) Heterogeneity of functional synaptic parameters among single release sites. Neuron 19:139-150.

Barski JJ, Hartmann J, Rose CR, Hoebeek F, Mörl K, Noll-Hussong M, De Zeeuw CI, Konnerth A, Meyer M (2003) Calbindin in cerebellar Purkinje cell is a critical determinant of the precision of motor coordination. J Neurosci. 23:3469-3477.

Baylor SM, Hollingworth S (1998) Model of sarcomeric Ca^{2+} movements, including ATP Ca^{2+} binding and diffusion, during activation of frog skeletal muscle. J Gen Physiol 112:297-316.

Berridge M J (1998) Neuronal calcium signaling. Neuron 21:13–26.

Blatow M, Caputi A, Burnashev N, Monyer H, Rozov A (2003) Ca^{2+} buffer saturation underlies paired pulse facilitation in calbindin-D28k-containing terminals. Neuron 38:79-88.

Burrone J, Neves G, Gomis A, Cooke A, Lagnado L (2002) Endogenous calcium buffers regulate fast exocytosis in the synaptic terminal of retinal bipolar cells. Neuron 33:101-112.

Caillard O, Moreno H, Schwaller B, Llano I, Celio M, Marty A (2000) Role of the calcium-binding protein parvalbumin in short-term synaptic plasticity. Proc Natl Acad Sci (USA) 97:13372-13377.

Celio MR (1986) Parvalbumin in most γ-aminobutyric acid-containing neurons of the rat cortex. Science 231:995-99.

Coutu P, Metzger M (2002) Optimal range for parvalbumin as relaxing agent in adult cardiac myocytes: gene transfer and mathematical modeling. Biophys J 82:2565-2579.

Dargan SL, Schwaller, Parker I (2004) Spatiotemporal patterning of IP3-mediated Ca^{2+} signals by Ca^{2+}-binding proteins. J Physiol(Lond) 556:447-461.

Eberhard M, Erne P (1991) Calcium binding to fluorescent calcium indicators: calcium green, calcium orange and calcium crimson. Biochem and Biophys Research Communications 180:209-215.

Eccles J C, Llinas R, Sasaki K (1966) The inhibitory interneurones within the cerebellar cortex. Exp Brain Res 1:1-16.

Edmonds B, Reyes R, Schwaller B, Roberts WM (2000) Calretinin modifies presynaptic calcium signaling in frog saccular hair cells. nature neuroscience 3:786-790.

Ekerot C-F, Jörntell H (2001) Parallel fibre receptive fields of Purkinje cells and interneurons are climbing fibre-specific. Eur J Neurosci 13:1303-1310.

Felmy F, Neher E, Schneggenburger R (2003) Probing the intracellular calcium sensitivity of transmitter release during synaptic facilitation. Neuron 37: 801-811.

Fierro L, Llano I (1996) High endogenous calcium buffering in Purkinje cells from rat cerebellar slices. J Physiol(Lond) 496:617–625.

Fierro L, DiPolo R, Llano I (1998) Intracellular calcium clearance in Purkinje cell somata from rat cerebellar slices. J Physiol(Lond) 510:499–512.

Forti L, Pouzat C, Llano I (2000) The spatial distribution of action potential-evoked Ca^{2+} signals in axons of developing rat cerebellar interneurons. J Physiol(Lond) 527:31-47.

Goda Y, Stevens CF (1994) Two components of transmitter release at a central synapse.

Proc Natl Acad Sci (USA) 91:12942-12946.

Haiech J, Derancourt J, Pechere JF, Demaille JG (1979) Magnesium and calcium binding to parvalbumins: evidence for differences between parvalbumins and an explanation of their relaxing function. Biochemistry 18:2752-2758.

Helmchen F, Borst JGJ, Sakmann B (1997) Calcium dynamics associated with a single action potential in a CNS presynaptic terminal. Biophysical J 72:1458-1471.

Jackson MB, Redman SJ (2003) Calcium dynamics, buffering, and buffer saturation in the boutons of dentate granule-cell axons in the Hilus. J Neurosc 23:1612-1624.

John LM, Mosquera-Caro M, Camacho P, Lechleiter JD (2001) Control of IP_3-mediated Ca^{2+}puffs in *Xenopus laevis* oocytes by the Ca^{2+}-binding protein parvalbumin. J Physiol(Lond) 535:3-16.

Kirischuk S, Grantyn R (2003) Intraterminal Ca^{2+} concentration and asynchronous transmitter release at single GABAergic boutons in rat collicular cultures. J Physiol(Lond) 548:753-764.

Koester HJ, Sakmann B (2000) Calcium dynamics associated with action potentials in single nerve terminals of pyramidal cells in layer 2/3 of the young rat neocortex J Physiol(Lond) 529:625-646.

Kosaka T, Kosaka K, Nakayama T, Hunziker W, Heizmann CW (1993). Axons and axon terminals of cerebellar Purkinje cells and basket cells have higher levels of parvalbumin immunoreactivity than somata and dendrites: quantitative analysis by immunogold labeling. Exp Brain Res 93:483-491.

Lee SH, Schwaller B, Neher E (2000) Kinetics of Ca^{2+} binding to parvalbumin in bovine chromaffin cells: implications for [Ca^{2+}] transients of neuronal dendrites. J Physiol(Lond) 525:419–432

Llano I, Marty A, Armstrong CM, Konnerth A (1991) Synaptic- and agonist-induced excitatory currents of Purkinje cells in rat cerebellar slices. J Physiol(Lond) 434:183-213.

Llano I, Tan Y, Caputo C (1997) Spatial heterogeneity of intracellular Ca^{2+} signals in axons of basket cells from rat cerebellar slices. J Physiol(Lond) 502:509-519.

Llano I, González J, Caputo C, Lai AF, Blayney LM, Tan YP, Marty A (2000) Ryanodine-sensitive Ca^{2+} stores underlie large amplitude miniature IPSCs and spontaneous presynaptic Ca^{2+} transients at Purkinje cell synapses. Nature Neurosci 3:1256-1265.

Llinás R, Sugimori, M, Silver RB (1992) Microdomains of high calcium concentration in a presynaptic terminal. Science 256:677-679.

Lu T, Trussell L O (2000) Inhibitory transmission mediated by asynchronous transmitter release. Neuron 28: 683-694.

Maeda H, Ellis-Davies GC, Ito K, Miyashita Y, Kasai H (1999) Supralinear Ca^{2+} signaling by cooperative and mobile Ca^{2+} buffering in Purkinje neurons. Neuron 24:989–1002.

Majewska A, Brown E, Ross J, Yuste R (2000) Mechanisms of calcium decay kinetics in hippocampal spines: role of spine calcium pumps and calcium diffusion through the spine neck in biochemical compartmentalization. J Neurosci 20:1722–1734.

Markram H, Roth A, Helmchen F (1998) Competitive calcium binding: Implications for dendritic calcium signaling. J Computational Neurosc 5:331-348.

Meinrenken CJ, Borst JG, Sakmann B (2003) Local routes revisited: the space and time dependence of the Ca^{2+} signal for phasic transmitter release at the rat calyx of Held J Physiol(Lond) 547:665-689.

Meyer AH, Katona I, Blatow M, Rozov, Monyer H (2002) *In vivo* labeling of parvalbumin-positive interneurons and analysis of electrical coupling in identified neurons. J Neurosci

22:7055-7064.

Neher E (1998) Usefulness and limitations of linear approximations to the understanding of Ca^{2+} signals. Cell Calcium 24:345-357.

Neher E, Augustine GJ (1992) Calcium gradients and buffers in bovine chromaffin J Physiol(Lond) 450:273–301.

Pozzan T, Rizzuto R, Volpe P, Meldolesi J (1994) Molecular and cellular physiology of intracellular calcium stores. Physiological reviews 74: 595-636.

Ricci AJ, Wu Y-C, Fettiplace R (1998) The endogenous calcium buffer and the time course of transducer adaptation in auditory hair cell. J Neurosc 18: 8261-8277.

Roberts WM (1993) Spatial calcium buffering in saccular hair cells. Nature 363:74-76.

Roberts WM (1994) Localization of calcium signals by a mobile calcium buffer in frog saccular hair cells. J Neurosc 14:3246-3262.

Rudy B, Chow A, Lau D, Amarillo Y, Ozaita A, Saganich M, Moreno H, Nadal MS, Hernandez-Pineda R, Hernandez-Cruz A, Erisir A, Leonard C, Vega-Zaenz de Meira E (1999) Contribution of Kv3 channels to neuronal excitability. In: Molecular and Functional Diversity of Ion Channels and Receptors. Annals of the New York Acad of Sciences, 868, pp304-343.

Schmidt H, Stiefel KM, Racay P, Schwaller B, Eilers J (2003a) Mutational analysis of dendritic Ca^{2+} kinetics in rodent Purkinje cells: role of parvalbumin and calbindin D_{28k}. J Physiol(Lond) 551:13-32.

Schmidt H, Brown EB, Schwaller B, Eilers J (2003b) Diffusional mobility of parvalbumin in spiny dendrites of cerebellar Purkinje neurons quantified by fluorescence recovery after photobleaching. Biophys J 84:2599-2608.

Schwaller B, Dick J, Dhoot G, Carroll S, Vrbova G, Nicoretta P, Pette D, Wyss A,

Bluethmann H, Hunziker W, Celio M (1999) Prolonged contraction-relaxation cycle of fast-twitch muscles in parvalbumin knockout mice. Am J Physiol 276:C395-C403.

Schwaller B, Meyer M, Schiffmann S (2002) "New" functions for "old" proteins: The role of the calcium-binding proteins calbindin D-28K, calretinin and parvalbumin, in cerebellar physiology. Studies with knockout mice. The Cerebellum 1:241-258.

Simon SM, Llinas RR (1985) Compartmentalization of the submembrane calcium activity during calcium influx and its significance in transmitter release. Biophys J 48:485-498.

Sinha SR, Wu L-G, Saggau P (1997) Presynaptic calcium dynamics and transmitter release evoked by single action potentials at mammalian central synapses. Biophys J 72: 637-651.

Smith C, Moser T, Xu T, Neher E (1998) Cytosolic Ca^{2+} acts by two separate pathways to modulate the supply of release-competent vesicles in chromaffin cells. Neuron 20:1243-1253.

Sultan F, Bower JM (1998) Quantitative Golgi study of the rat cerebellar molecular layer interneurons using principal component analysis. J Comp Neurol 393: 353-373.

Tan YP, Llano I (1999) Modulation by K^+ channels of action potential evoked intracellular Ca^{2+} rises in rat cerebellar basket cell axons. J Physiol(Lond) 520:65-78.

Tan YP, Llano I, Hopt A, Würriehausen F, Neher E (1999) Fast scanning and efficient photodetection in a simple two-photon microscope. J Neuroscience Methods 92:123-135.

Van der Kloot W, Molgo J (1993) Quantal acetlycholine release at the vertebrate neuromuscular junction. Physiol Rev 74: 899-991.

Vincent P, Marty A (1996) Fluctuations of inhibitory postsynaptic currents in Purkinje cells from rat cerebellar slices. J Physiol(Lond) 494:183-199.

Westerblad H, Lannergren J (1991) Slowing of relaxation during fatigue in single mouse

muscle fibres. J Physiol(Lond) 434:323-36.

Zhang L, Goldman JE (1996) Generation of cerebellar interneurons from dividing progenitors in white matter. Neuron 16:47-54.

Zucker RS, Regehr WG (2002) Short-term synaptic plasticity. Ann Rev Physiol 64:355-405.

Table I: Kinetic parameters used for simulations.

Data for Calcium Green-1. ** Estimated from *in vitro* calibrations performed as detailed in Methods. * The value used is the one given in this paper for mammalian α–PV.

Definition	Symbol	Value	Source
OG1 with Ca^{2+}	$k_{on,CaD}$	8.24 x 10^8 $M^{-1}s^{-1}$	calculated
	$k_{off,CaD}$	140 s^{-1}	Eberhard and Erne (1991) *
	$k_{D,CaD}$	170 nM	Measured **
PV with Ca^{2+}	$k_{on,PVCa}$	3.64 x 10^8 $M^{-1}s^{-1}$	Coutu *et al.* (2002)
	$k_{off,PVCa}$	4.03 s^{-1}	id.
	$k_{D,PVCa}$	11 nM	id.
PV with Mg^{2+}	$k_{on,PVMg}$	1.42 x 10^5 $M^{-1}s^{-1}$	calculated
	$k_{off,PVMg}$	2.2 s^{-1}	Westerblad and Lannergren (1991)
	$k_{D,PVMg}$	15 µM	Haiech *et al.* (1979) ***
ATP with Ca^{2+}	$k_{on,ATPCa}$	1.5 x 10^8 $M^{-1}s^{-1}$	Baylor and Hollingworth (1998)
	$k_{off,ATPCa}$	3 x 10^4 s^{-1}	id.
	$k_{D,ATPCa}$	200 µM	id.
ATP with Mg^{2+}	$k_{on,ATPMg}$	1.5 x 10^6 $M^{-1}s^{-1}$	Baylor and Hollingworth (1998)
	$k_{off,ATPMg}$	150 s^{-1}	id.
	$k_{D,ATPMg}$	100 µM	id.

FIGURE LEGENDS

Figure 1. Age- and interneuron subtype-dependent changes in Ca_i signaling at presynaptic varicosities. A1, A2: 2-photon pseudocolor images of the OG1 Ca^{2+}-dependent fluorescence from a PN11 stellate cell axon at rest (A1) and at the peak of the response to a 50 Hz train of 4 APs (A2). A3: Time course of the relative changes in fluorescence ($\Delta F/F_O$) in ROIs identified by arrows in A2. Superimposed on the data traces are the fits of the decay phase by single (blue dotted lines) and double exponential functions (red dotted lines), which in this case are equivalent indicating that the decay kinetics are well described by a single exponential. Note that the data traces as well as the corresponding fits return to pre-stimulus levels. B1-B3: similar analysis for the AP-evoked Ca_i rises in a PN12 basket cell axon. For this type of interneuron, the decay time course is fast and follows a double exponential function. C1-C3: At PN21, stellate cell axonal Ca_i rises have evolved towards a fast and biphasic decay. C4 presents the AP-evoked current traces for this neuron. D: Comparison of the average decay time course, estimated as the time to decay to 50% of peak amplitude, for stellate and basket cells of the two age groups. The analysis contains data from 6 basket and 7 stellate cells at PN10-12 and 5 basket and 6 stellate cells at PN19-21. The bars denote the s.e.m. ANOVA test for this data yields $F= 26.29$ ($p<0.0001$). * indicate groups which are statistically significant using Student's t-test.

Figure 2. Developmental profile of PV expression in cerebellar interneurons. A1, A2 : Confocal images from slices of a PN10 (A1) and a PN20 (A2) mouse cerebellum. Double staining with PV and CB antibodies, performed as described in Methods. Due to the choice of secondary antibodies (see methods) PV-containing cells show as green in these images, whereas cells expressing PV and CB appear yellow. Thus, the prominent yellow stain identifies Purkinje cells, well known to express both CBPs, and green identifies

interneurons, which express PV but not CB. At PN10, PV-containing interneurons are located primarily in close proximity to the Purkinje cell layer, and can thus be identified as basket cells. At PN20, in contrast, numerous PV-containing interneurons are visible in the middle molecular layers, location of stellate cells. A3: evolution of the density of PV positive interneurons as a function of age. Bars represent the s.e.m. A4: maximal excursion of PV expressing interneurons in the molecular layer as a function of age. The blue bars correspond to the height of the molecular layer at each age. B: Age-dependent increase in the total quantity of PV in mouse cerebellum, as determined by quantitative Western blots parallels the immunocytochemical observations. C1, C2 : Confocal images from slices of a PN12 (C1) and a PN20 (C2) mouse cerebellum. Double staining with GABA and CB antibodies. MLIs, appear green and are seen to be present throughout the molecular layer since PN12. C3: quantitative comparisons for the evolution of PV and GABA expression between PN12 and PN20.

Figure 3. Absence of PV cancels the age-dependent changes in presynaptic Ca_i signaling. A1: resting fluorescence of an axonal region of a PN12 basket interneuron from a PV(-/-) mouse. A2: corresponding image at the peak response to a 4 AP train. A3: In contrast to the WT phenotype at this age, the time course to the AP-evoked Ca_i signals acquired at the varicosities indicated by the arrows in A2, is slow and well described by a single exponential (blue dotted traces). Thus PV removal converts the Ca_i decay kinetics in MLIs back to the slow monophasic decay that is observed at PN10-12 in the WT. A4: Action potential currents were not different in PV(-/-) mice and in WT mice (compare with Fig. 1C4). B: Comparison of the average decay time course indicates significant differences between WT and PV(-/-) basket cells at PN10-12 but no difference for the stellate cells of this age group. At PN19-21, deletion of PV(-/-) also leads to a significant

change in decay time course. The number of cells for the WT groups are: 6, 7 and 11 for the PN10-12 basket cells, PN10-12 stellate cells and PN19-21 interneurons respectively. The PV(-/-) groups include 3 basket cells and 3 stellate cells at PN10-12 and 10 interneurons at PN19-21. ANOVA test for this data yields $F=10.20$ ($p<0.0001$). $*$ indicate groups which are statistically significant using Student's t-test.

Figure 4. Measurements of AP-evoked Ca_i with 20 μM OG1, and estimation of fast endogenous buffer capacity. A1, A2: Resting and peak Ca_i images (following a 4-AP stimulus) from an axon dialyzed with 20 μM OG1 (PN19 stellate cell, from a PV(-/-) mouse). A3: Time course of decay for the 2 ROIs depicted in a2 (black and red traces). Both decay time courses could be approximated with a single exponential (blue dotted lines; time constants, 0.58 and 0.69 s). Average peak $\Delta F/Fo$ and 50% decay time from similar experiments (4 cells) were: 204±28% and 0.32±0.10 s, respectively B: Average decay time course for PV(-/-) data from experiments performed with 20 μM (black trace) and 100 μM OG1 (blue trace) are compared with numerical simulations (red and yellow traces, for low and high dye concentration, respectively). The best approximations to the experimental data were obtained with a Ca load of 11 μM/AP, extrusion/influx kinetic constants $k_1=550\ s^{-1}$ and $k_{-1}=0.011\ s^{-1}$ and an endogenous buffer capability equivalent to 60 μM OG1. The same simulation parameters fail to approximate the 20 μM OG1 experimental data if the endogenous buffer is not included (green trace).

Figure 5. Determination of the endogenous PV concentration. A: Numerical simulations of the time course of decay of Ca_i signals for PV concentrations ranging from 0 to 300 μM, obtained using the simulation parameters which gave the best approximation to the PV(-/-) data, namely, a Ca^{2+} load of 11 μM /AP, extrusion/influx kinetic constants

k_1=550 s^{-1} and k_{-1}=0.011 s^{-1} and an endogenous buffer capability equivalent to 60 μM OG1. Note that, regardless of the PV concentration, there is a large discrepancy with the average decay obtained in WT, PN19-21 MLIs (dotted black trace). B: Family of simulations performed with extrusion/influx kinetic constants increased by a factor of 2 (k_1=1100 s^{-1} and k_{-1}=0.022 s^{-1}). A concentration of 150 μM closely approximates the average WT data (dotted black trace).

Figure 6. The time course of Ca_i governs delayed transmitter release at MLI-MLI synapses. A: Predicted averaged Ca_i time course. The black solid trace represents the simulated Ca_i decay following a 50 Hz train of 4 APs, in the absence of calcium indicator. Simulation parameters: Ca load of 11 μM/AP, 150 μM PV, 60 μM OG1-like buffer and extrusion kinetic constants k_1=1100 s^{-1} and k_{-1}=0.022 s^{-1}. This Ca_i decay is characterized by a bi-exponential decay (τf: 39 ms, τs: 626 ms; corresponding amplitude coefficients : 144 and 29 nM). The black dotted trace presents the response to a 50 Hz train of 10 APs. The Ca_i decay for the PV-free conditions (red solid trace: 4AP train; dotted red trace : 10AP train), used the following simulation parameters: Ca^{2+} load of 11 μM/AP; 60 μM OG1-like buffer; extrusion rates: k_1=550 s^{-1} and k_{-1}=0.011 s^{-1}. Traces have been truncated at 250 nM in order to highlight differences in the slow decay phase. B: Comparison of delayed transmitter release in WT and PV(-/-) mice. B1: representative recording of currents obtained from a PN20 WT MLI. The arrow indicates the onset of a 50 Hz train of 10 presynaptic stimulations. B2: expanded view of the recording during the stimulation train, as denoted by the dashed line with arrow in B1. B3, B4: representative experiment from a PN20 PV(-/-) interneuron. Glutamatergic activity has been blocked as detailed in Methods. C1, C2: Histograms of the temporal evolution of the mean frequency of synaptic events over the pre-stimulus frequency, pooled from 9 WT and 6 PV(-/-)

interneurons (PN19-21). Error bars represent the s.e.m. Time 0 corresponds to the end of the extracellular stimulation. The blue traces display the Ca_i time course calculated for a 50 Hz train of 10 APs, from Fig. 6A. Values for the WT group, were significantly different from 1 ($p<0.05$) for all time bins. For the PV(-/-) group, only the first 2 time bins have a similar statistical significance.

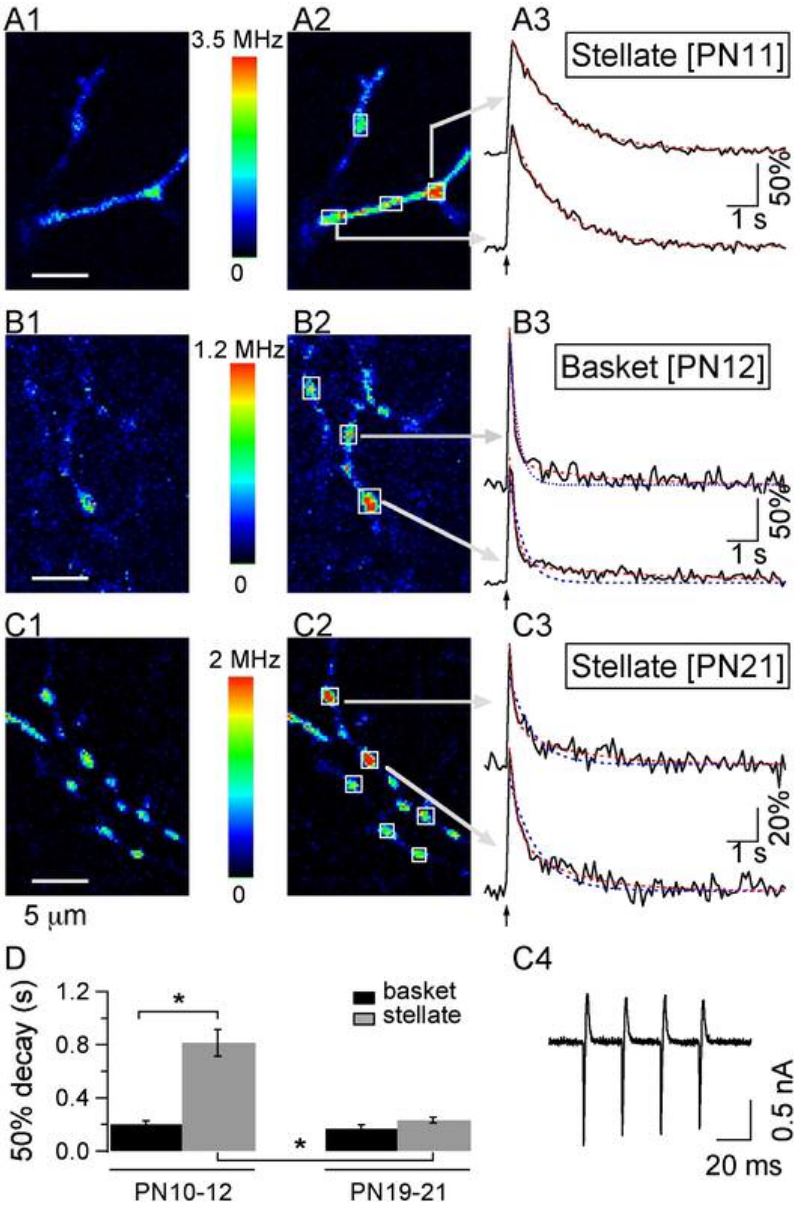

89x135mm (150 x 150 DPI)

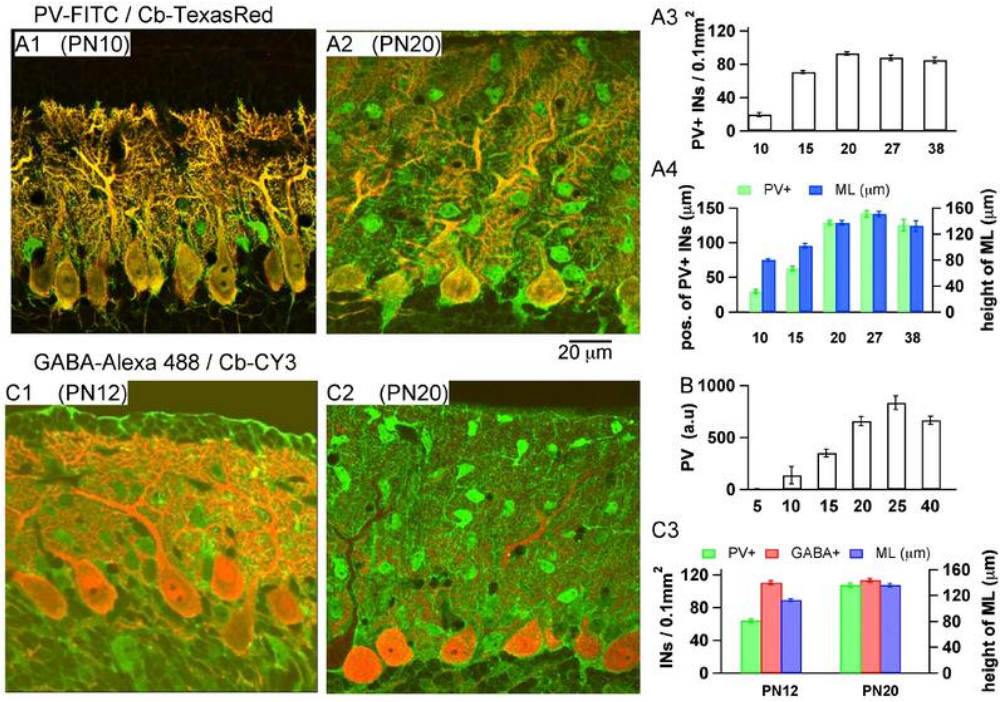

134x94mm (150 x 150 DPI)

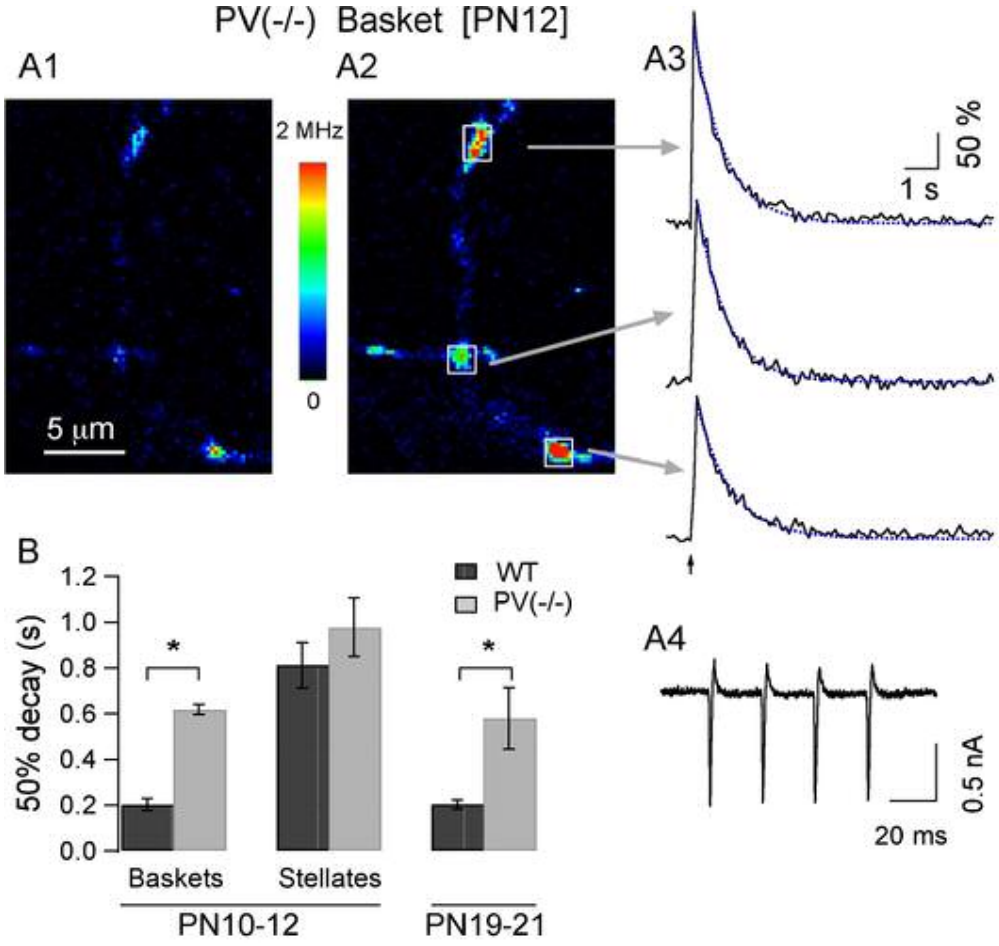

89x84mm (150 x 150 DPI)

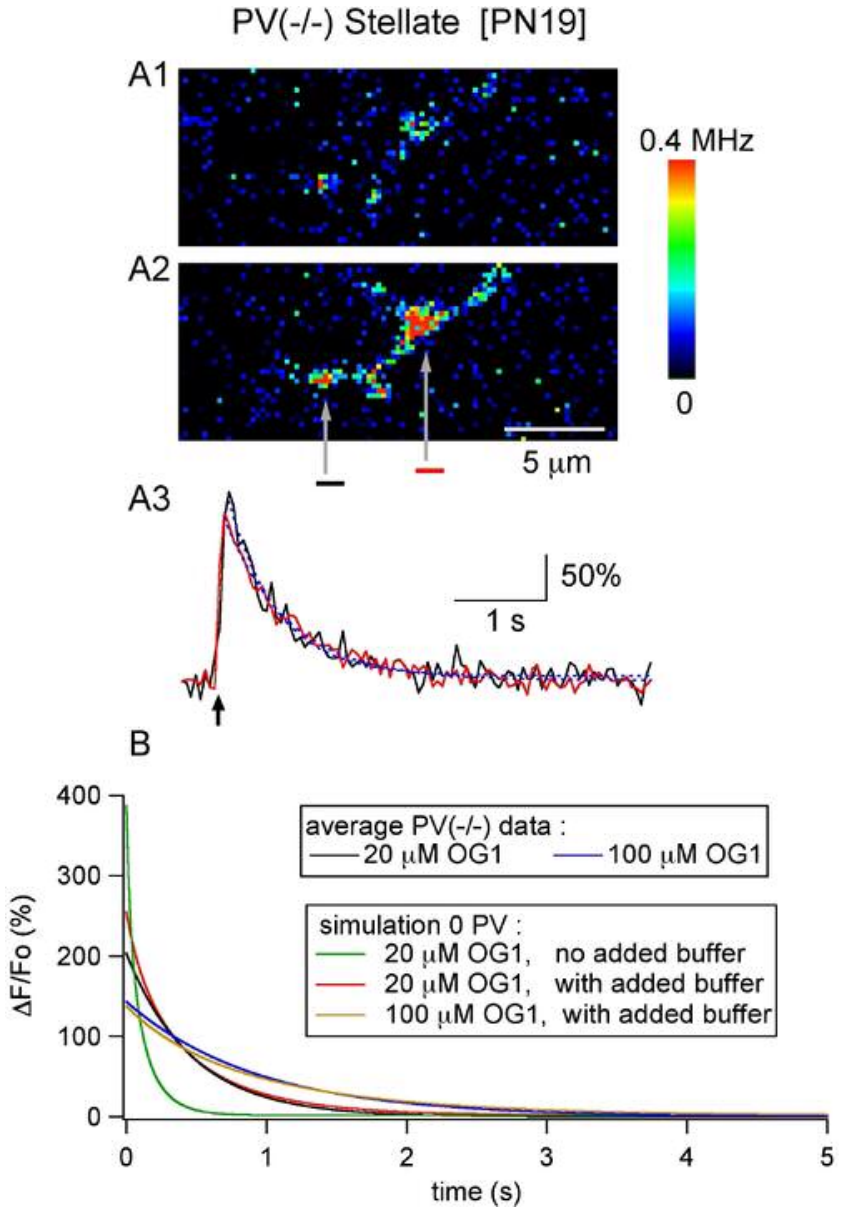

84x121mm (150 x 150 DPI)

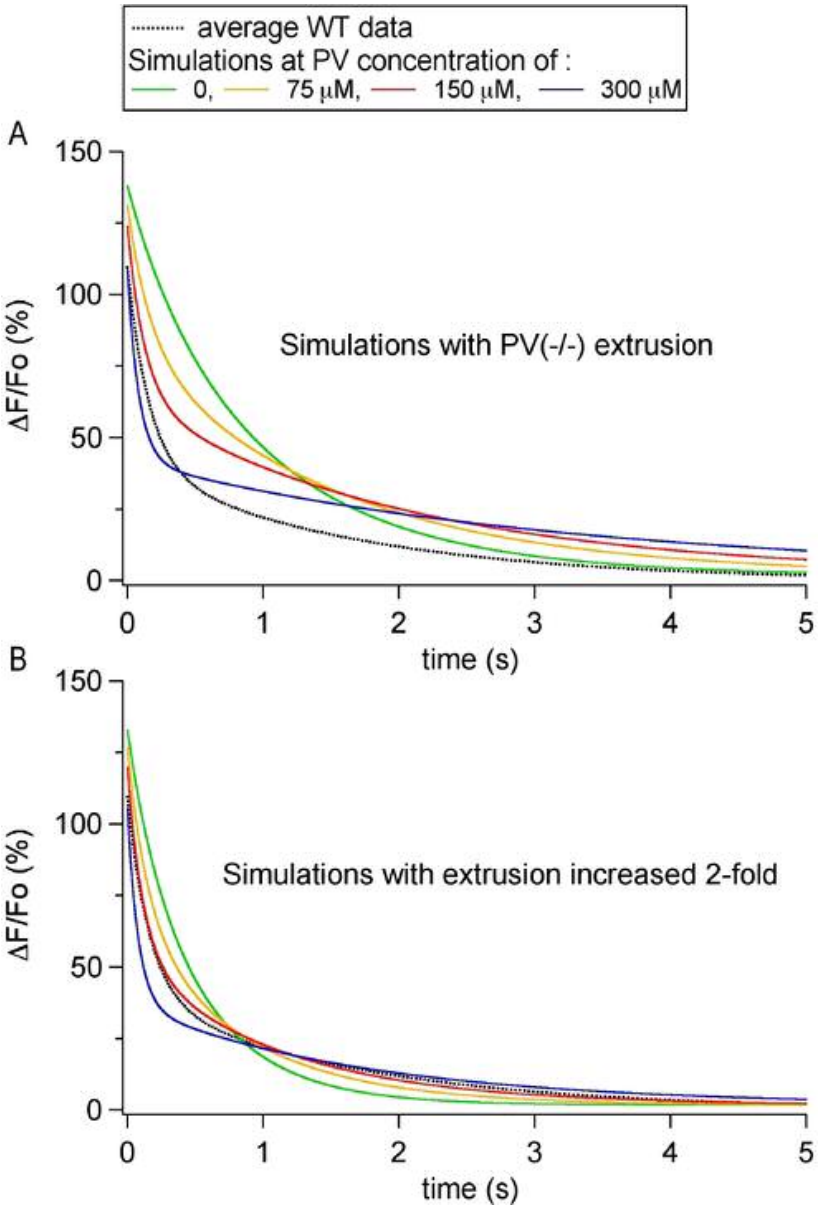

83x122mm (150 x 150 DPI)

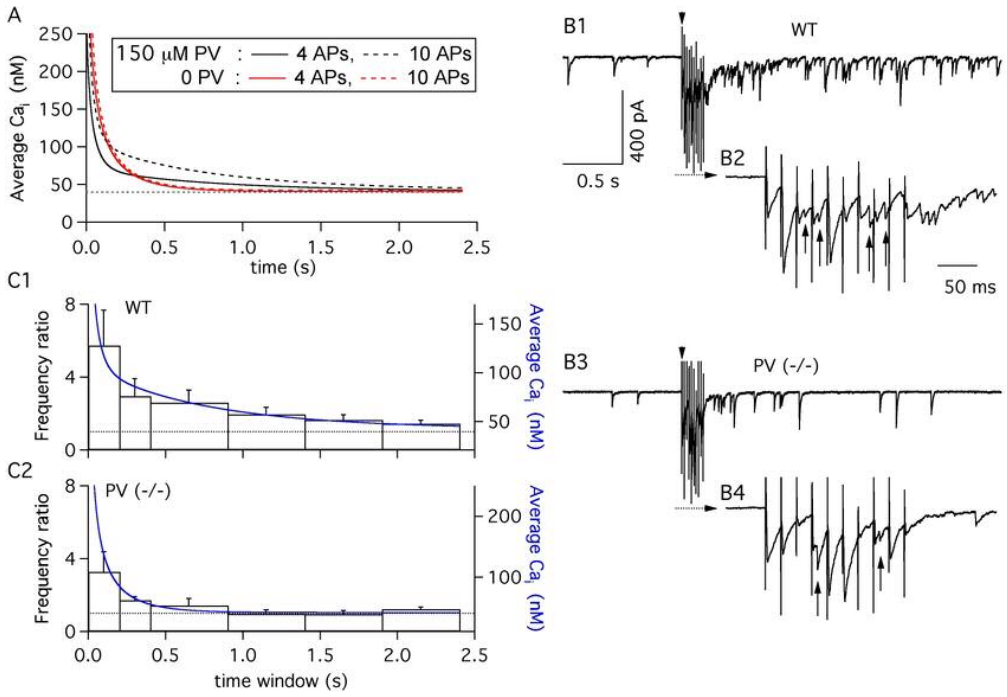

143x98mm (150 x 150 DPI)